ARTICLE

Check for updates

Developing sustainable FeTi alloys for hydrogen storage by recycling

Yuanyuan Shang[1], Shaofei Liu[2], Zhida Liang[3,4], Florian Pyczak[3], Zhifeng Lei [5], Tim Heidenreich[1],
Alexander Schökel [6], Ji-jung Kai [2,7], Gökhan Gizer[1], Martin Dornheim [1], Thomas Klassen[1,8] &
Claudio Pistidda [1✉]

Intermetallic alloys such as FeTi have attracted ever-growing attention as a safe and efficient hydrogen storage medium. However, the utilization of high-purity metals for the synthesis of such materials poses considerable concerns over the environmental sustainability of their large-scale production. Here, we report an approach for synthesizing FeTi from industrial scraps of iron (steels C45 and 316 L) and titanium (Ti alloy Grade 2) to reduce the carbon footprint associated with FeTi alloy synthesis, without compromising their hydrogen storage properties. At 50 °C and a pressure of 0 to 100 bar, the alloys obtained by using C45-Ti Grade 2 and 316L-Ti Grade 2 can absorb a maximum amount of hydrogen of 1.61 wt.% and 1.50 wt.%, respectively. Moreover, depending on the type of steel utilized, the thermo-dynamic properties can be modified. Our findings pave a pathway for developing high-performance, environmentally-sustainable FeTi alloys for hydrogen storage purposes using industrial metal wastes.

[1] Department of Materials Design, Institute of Hydrogen Technology, Helmholtz-Zentrum hereon GmbH, 21502 Geesthacht, Germany. [2] Department of Mechanical Engineering, City University of Hong Kong, 999077 Hong Kong, China. [3] Department of Metal Physics, Institute of Materials Physics, Helmholtz-Zentrum hereon GmbH, 21502 Geesthacht, Germany. [4] Department of Materials Science and Metallurgy, Cambridge University, Cambridge CB3 0FS, UK. [5] College of Materials Science and Engineering, Hunan University, 410082 Changsha, China. [6] Deutsches Elektronen-Synchrotron DESY, Notkestr. 85, 22607 Hamburg, Germany. [7] Center for Advanced Nuclear Safety and Sustainable Development, City University of Hong Kong, Hong Kong, China. [8] Helmut Schmidt University, Holstenhofweg 85, 22043 Hamburg, Germany. ✉email: claudio.pistidda@hereon.de

The possibility to reversibly store hydrogen in FeTi alloys was first reported by Reilly and Wiswall in 1974[1]. This B2-structured intermetallic compound possesses gravimetric and volumetric hydrogen storage properties (1.87 wt.% and 105 kg H_2 m^{-3} at 25 °C under 50 bar H_2)[2] that make it an appealing candidate for storing hydrogen in stationary applications. In FeTi the hydrogen is interstitially stored in tetrahedral and octahedral sites[3]. The reaction enthalpy and entropy associated with the release of hydrogen from FeTi are equal to 28.1 kJ mol^{-1} H_2 and 106 J K^{-1} mol^{-1} H_2, respectively[1]. This entails an equilibrium temperature of −8.0 °C at 1 bar of hydrogen pressure, which is particularly interesting when considering the coupling of a potential FeTi-based hydrogen storage system with a polymer electrolyte membrane (PEM) fuel cell system[4]. Despite the promising hydrogen storage capacity, issues related to the material activation and tilted hydrogen absorption/desorption plateau pressure limit the utilization of pure FeTi in commercial applications[5–10]. In recent years, many attempts to enhance the FeTi hydrogen storage properties have been carried out mostly by elemental substitution. By adding A-type (Ti) elements like Nb, Zr, and V into the system, the strength of the hydrogen-metal bonds can be modified, while the addition of B-type (Fe) elements such as Cu, Ni, Co, Mn, and Al can improve the electrocatalytic activity, thus facilitating the activation process[11,12]. Additionally, alloying with elements such as Mn and V allows reducing the hydrogenation/dehydrogenation plateau pressure slope[13–15]. As an example, by substituting Fe by Mn, the lattice constant of FeTi increases, resulting in lower equilibrium pressure, a smoothed plateau, and decreased hysteresis[13]. What's more, the addition of Mn induces the formation of secondary phases, which could act as a channel for hydrogen absorption, leading to a milder activation condition[7,16].

As the result of the many years of studies on FeTi-based materials and due to their specific hydrogen storage properties, nowadays these intermetallic compounds are one of the few materials utilized for commercial hydrogen storage applications[17]. Considering the actual political and environmental situation, in the upcoming years, the development of large-scale FeTi-based hydrogen storage systems will be necessary as the consequence of a shift from a fossil fuel-based to a renewable energy source-based economy. Such transition poses significant economical and environmental sustainability questions on the so-far utilized approach for the production of FeTi-based materials. Currently, FeTi-based alloys are produced using Fe and Ti of high purity, i.e., 99.5% to 99.999%[18–23]. From an economical point of view the utilization of such high-purity metal sources for the mass production of hydrogen storage systems is prohibitory as the cost of Fe with a purity of 99.99%[24] is 7 US\$ kg^{-1}, and the cost of 99.7 to 99.99% pure Ti[25,26] is 10.5 to 35.3 US\$ kg^{-1}. From the environmental point of view also the utilization of high-purity metal sources is detrimental as the Fe production leads to the emission in the atmosphere of a number of CO_2 equivalents (CO_2-eq) equal to 1.5 kg[27] CO_2-eq kg^{-1}. The environmental impact of the production of Ti is even more dire as it brings about the emission of a number of CO_2-eq equal to 8.1 kg[27] CO_2-eq kg^{-1}. In this regard, finding alternative raw material sources capable of reducing the cost and the environmental impact is a key step towards the development of sustainable FeTi alloys for large-scale and widespread hydrogen storage applications. With steels being the most widely used alloys in the world, a considerable amount of end-of-life waste alloys is accumulated in scrapyards[28–30]. These alloys have high embodied energy[31], ca. 25–28 MJ kg^{-1}, and their accumulation causes considerable energy losses when not recycled. In addition, although the end-of-life recycling input rate of Ti can reach 90%[32], it still results in a considerable loss of Ti resources.

Here, we demonstrate a sustainable method for synthesizing FeTi alloys for hydrogen storage applications from waste steels and Ti alloy scraps. FeTi alloys were obtained by replacing pure Fe and Ti with the scraps of two typical types of steel (C45 and 316 L) and 3.7035 Titanium Grade 2 alloy (Gr2), respectively. The hydrogen storage properties measured for the synthesized C45-Gr2 FeTi and 316L-Gr2 FeTi are comparable in terms of hydrogen storage capacity and reaction kinetics for the temperature and hydrogen pressure ranges investigated in this work.

Results

Structural characterizations. The pure FeTi, C45-Gr2 FeTi, and 316L-Gr2 FeTi ingots with a dimension of Φ3 mm × 30 mm were prepared by arc melting and subsequent suction casting. The compositions of the utilized steels and Ti alloy are summarized in Supplementary Tables 1–3. The C45 steel contains around 0.42–0.50 wt.% of C, 0.5–0.8 wt.% of Mn, a maximum of 0.63 wt.% of Ni+Cr+Mo, and a maximum of 0.4 wt.% of Si. The 316 L steel contains 10–14 wt.% of Ni, 16–18 wt.% of Cr, 2–3 wt.% of Mo, a maximum of 0.75 wt.% of Si, and maximum 2 wt.% of Mn. The 3.7035 Titanium Grade 2 contains maximum 0.3 wt.% of Fe, maximum 0.08 wt.% of C, and maximum 0.25 wt.% of O. High energy X-ray diffraction (HEXRD) and scanning electron microscopy (SEM) techniques were used to characterize the microstructures of the bulk pure FeTi, C45-Gr2 FeTi, and 316L-Gr2 FeTi alloys after casting. According to the Rietveld refinement analysis in Supplementary Fig. 1, the main phase in pure FeTi is FeTi (98.6 ± 0.4 %) with a lattice constant of $a = 2.9788 \pm 0.0004$ Å, and around 1.4 ± 0.1 % of FeTi$_2$ phase ($a = 11.3067 \pm 0.0035$ Å) can also be detected. The SEM images in Fig. 1b, c and energy dispersive X-ray (EDX) results in Supplementary Fig. 4 confirm the presence of the FeTi and FeTi$_2$ phases. Interestingly, for the C45-Gr2 FeTi alloy (Fig. 1d and Supplementary Fig. 2), except for 96.0 ± 0.4 % of the main FeTi phase ($a = 2.9778 \pm 0.0002$ Å), 2.8 ± 0.1 % of Fe$_2$Ti precipitates can be found near the grain boundaries, and 1.2 ± 0.1 % of TiC can be detected, which has a smaller size than the Fe$_2$Ti precipitates, as proved by the SEM images in Fig. 1e, f. It is clear that the grain size of the C45-Gr2 FeTi is much smaller than that of the pure FeTi, as can be seen in Supplementary Fig. 5. For the 316L-Gr2 FeTi (Fig. 1g), the Rietveld refinement results (Supplementary Fig. 3) show that the main phase is still FeTi (49.3 ± 0.3 %), however, the lattice constant increased to $a = 3.1057 \pm 0.0004$ Å, which indicates that the Cr, Ni, and other elements in 316L-Gr2 steel may have substituted the Fe in the FeTi alloy thus resulting in a variation in the lattice constant. SEM images in Fig. 1h, i and EDX analysis in Supplementary Fig. 6 reveal that the elemental composition of the FeTi matrix in 316L-Gr2 alloy is around 35 at.% of Fe, 10 at.% of Cr, 5 at.% of Ni, and 50 at.% of Ti, whereas the Fe may be substituted by Cr and Ni and can be written as (Fe$_{0.7}$Cr$_{0.2}$Ni$_{0.1}$)Ti. The Rietveld refinement analysis in Supplementary Fig. 3 shows that the remaining phases are 31.3 ± 0.4 % of CrFeTi and 19.4 ± 0.8 % of Fe$_{0.2}$Ti$_{0.8}$, while the EDX results (Supplementary Fig. 6) suggest that the elemental compositions of the CrFeTi phase are around 20 at.% of Cr, 40 at.% of Fe, and 40 at.% of Ti, which can be written as Cr$_{0.2}$Fe$_{0.4}$Ti$_{0.8}$. In addition, the elemental composition of the Fe$_{0.2}$Ti$_{0.8}$ phase is ~20 at.% of Fe, 8 at.% of Cr, 8 at.% of Ni, and 64 at.% of Ti, indicating that the exact composition could be Fe$_{0.2}$Cr$_{0.08}$Ni$_{0.08}$Ti$_{0.64}$.

Figure 2a shows the transmission electron microscopy (TEM) results of the pure FeTi alloy. The selected area electron diffraction (SAED) patterns show that area 1 and area 2 in the bright field image correspond to FeTi and FeTi$_2$ phases, respectively. The quantitative EDX line profiles in Fig. 2b
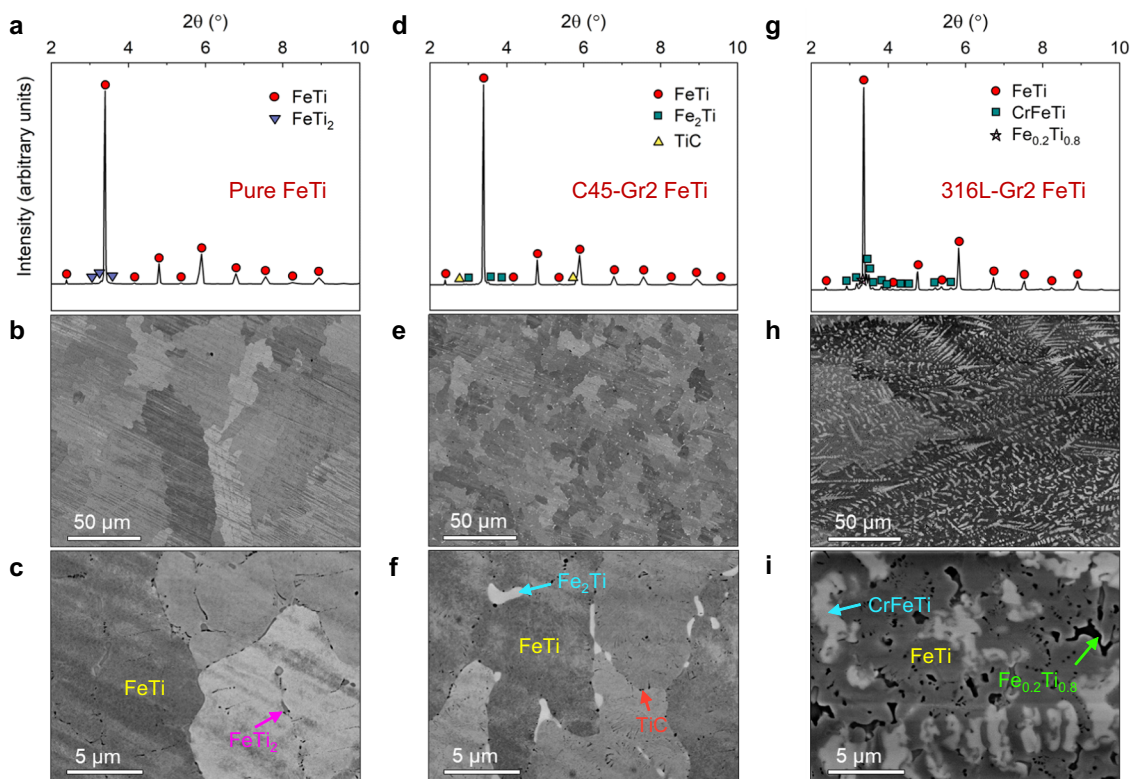
Fig. 1 Microstructures of as-cast pure FeTi, C45-Gr2 FeTi, and 316L-Gr2 FeTi alloys. a–c HEXRD ($\lambda = 0.124$ Å) patterns and corresponding SEM images of pure FeTi. **d–f** HEXRD ($\lambda = 0.124$ Å) patterns and corresponding SEM images of C45-Gr2 FeTi. **g–i** HEXRD ($\lambda = 0.124$ Å) patterns and corresponding SEM images of 316L-Gr2 FeTi, respectively.

demonstrate the existence of FeTi and FeTi$_2$ phases, which are also in good agreement with the HEXRD result (Fig. 1a) and SEM-EDX results (Supplementary Fig. 4). For the C45-Gr2 FeTi, as can be seen in Fig. 2c, d, area 1, area 2, and area 3 correspond to FeTi, TiC, and Fe$_2$Ti phases, respectively, which is also confirmed by the EDX line-scan analysis in Fig. 2e, f. These results are also consistent with the SEM-EDX data (see Supplementary Fig. 5). The TEM results in Fig. 2g for 316L-Gr2 FeTi show that the matrix (area 1) of the alloy is FeTi, but around 15 at.% of Fe is substituted by Ni and Cr, as can be seen in the EDX results (Fig. 2h). The SAED pattern shows that area 2 in the bight field image is likely to be Fe$_{0.2}$Ti$_{0.8}$, which is confirmed both by the TEM-EDX results (Fig. 2h) and by the SEM-EDX results (Supplementary Fig. 6). Note that although the EDX data from SEM may slightly differ from those from TEM, indicating that the elemental distribution fluctuates for this phase, the SAED results and HEXRD analysis confirm the existence of Fe$_{0.2}$Ti$_{0.8}$ phase. Although the O content in the Ti alloy scraps is around 0.25 wt.% and additional oxygen was certainly present at the surface of the starting material, in the synthesized alloys, no oxide species were detected via HEXRD, SEM, and TEM techniques. A possible explanation might involve the release of molecular oxygen during the arc melting process, oxygen that then forms a nanometric oxide layer on the upper surface of the ingots. This hypothesis is supported by the fact that the obtained material must be activated before it can begin to absorb hydrogen. The phase compositions for the three alloys in this work are summarized in Table 1. FeTi and Fe$_2$Ti are stable equilibrium phases. In the literature, it is reported that Fe$_2$Ti is likely to form when C or B are added to the FeTi system[33], and this well agrees with our finding on the C45-Gr2 FeTi alloy. The metastable phase FeTi$_2$ can only be formed at temperatures higher than 1000 °C, as at lower temperatures FeTi$_2$ decomposes into FeTi and Ti[1]. Thus,

the existence of the FeTi$_2$ phase at ambient temperature in the pure FeTi is most likely the result of the fast cooling of the melt after the arc melting procedure. As Patel et al. reported, the addition of Zr or Mn can also induce the formation of the FeTi$_2$ phase[34]. The formation of the Fe$_{0.2}$Ti$_{0.8}$ phase occurs when the starting material is 40 at.% of Fe and 60 at.% of Ti[35], which is also similar to the case of 316L-Gr2 FeTi. Therefore, here we can propose the hypothesis that the Fe$_2$Ti might be formed when some interstitial elements are added into the system, whereas the interstitial elements might form some Ti-based compounds with Ti, and then the rest of Ti might form Fe$_2$Ti phase with Fe. Similarly, when adding substitutional elements into the system, the formation of a metastable FeTi$_2$ phase could be induced. In addition, by adding excess Ti into the system, e.g., the atomic ratio between Ti and Fe is greater than 1, the Fe$_{0.2}$Ti$_{0.8}$ phase could generate.

Hydrogen storage properties. To check the hydrogen storage properties of the prepared alloys, the ingots were hand crushed into powders and sieved through a 125 μm sieve. The hydrogen storage thermodynamic properties of the three alloys after activation are shown in Fig. 3. As can be seen in the pressure-composition isotherm (PCI) curves in Fig. 3a, the total hydrogen storage capacity of pure FeTi ranges from 1.64 wt.% at 40 °C to 1.71 wt.% of H$_2$ at 70 °C (100 bar of H$_2$). While the values for C45-Gr2 FeTi range from 1.62 wt.% at 40 °C to 1.58 wt.% at 70 °C under the same condition (Fig. 3d). For the 316L-Gr2 FeTi, the hydrogen storage capacity is in the range of 1.52 wt.% at 70 °C to 1.70 wt.% at 150 °C under 100 bar of H$_2$ (Fig. 3g). The results indicate that by replacing high-purity raw materials with steel and Ti alloy scraps, the maximum storage capacities of the synthesized FeTi are only slightly decreased. As shown in Fig. 3e, the
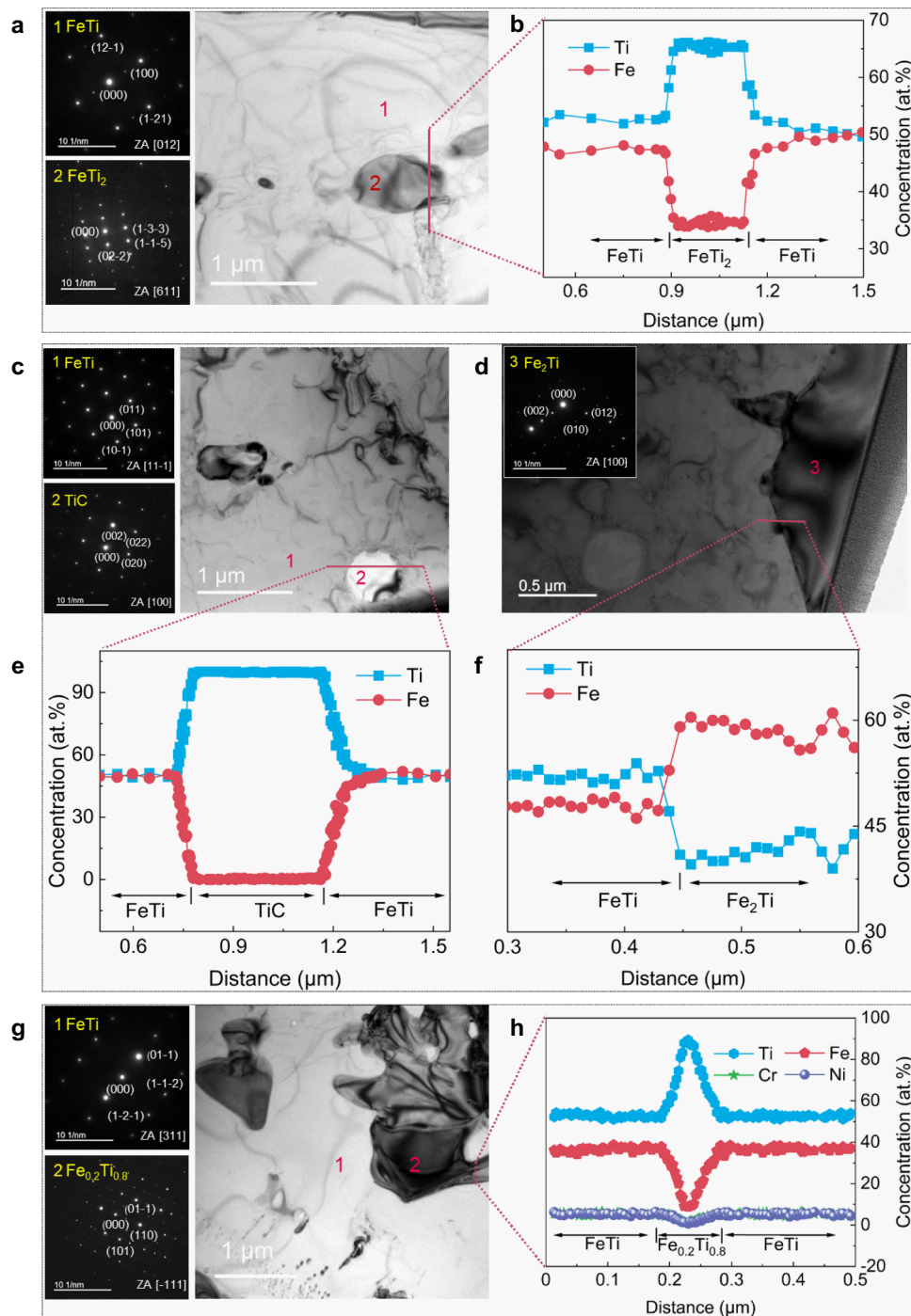
Fig. 2 TEM results of as-cast pure FeTi, C45-Gr2 FeTi, and 316L-Gr2 FeTi alloys. a Bright-field image and corresponding SAED images, and **b** line EDX results of pure FeTi. **c**, **d** Bright-field image, and corresponding SAED images, and **e**, **f** Line EDX results of C45-Gr2 FeTi. **g** Bright-field image and corresponding SAED images, and **h** Line EDX results of 316L-Gr2 FeTi.

hydrogenation ΔH_{abs} and ΔS_{abs} of C45-Gr2 FeTi were calculated to be -23.9 ± 0.1 kJ mol^{-1} and -98.6 ± 0.4 J K^{-1} mol^{-1}, respectively, while the dehydrogenation ΔH_{des} and ΔS_{des} are 26.9 ± 0.4 kJ mol^{-1} and 102.5 ± 1.2 J K^{-1} mol^{-1}, respectively. These values (absolute) are slightly lower than the values for pure FeTi ($\Delta H_{abs} = -24.6 \pm 0.3$ kJ mol^{-1} and $\Delta S_{abs} = -100.8 \pm 1.0$ J K^{-1} mol^{-1}, $\Delta H_{des} = 27.4 \pm 0.4$ kJ mol^{-1} and $\Delta S_{des} = 104.2 \pm 1.3$ J K^{-1} mol^{-1}) in Fig. 3b, indicating that the hydrogenated C45-Gr2 FeTi is thermodynamically less stable than the pure FeTi. Besides this first plateau, there is a second plateau present in both the pure and C45-Gr2 FeTi alloys. As reported in the literature[11,16], the first plateau is

related to the coexistence of α-phase and β-phase, of which the α-phase is a solid solution of hydrogen in FeTi, and the β-phase is a monohydride phase. The second plateau corresponds to the coexistence of β-phase and γ-phase, whereas the γ-phase is a dihydride phase. It is clearly shown that the carbon in the C45 steel does not significantly influence the coexistence of the β-phase and γ-phase. Distinctly, as can be seen in Fig. 3g, the plateau pressure for the 316L-Gr2 FeTi is significantly decreased and the second plateau vanishes for 316L-Gr2 FeTi alloy. The ΔH and ΔS values were calculated to be $\Delta H_{abs} = -35.0 \pm 0.7$ kJ mol^{-1} and $\Delta S_{abs} = -93.6 \pm 0.2$ J K^{-1} mol^{-1}, $\Delta H_{des} = 34.4 \pm 2.5$ kJ mol^{-1}, and $\Delta S_{des} = 92.6 \pm 0.7$ J K^{-1} mol^{-1},

Table 1 Phase constitutions of pure FeTi, C45-Gr2 FeTi, and 316L-Gr2 FeTi alloys.

| Alloy	Phase	Crystal structure	Percentage (wt.%)	Lattice constant (Å)	EDX analysis (atomic ratio)
Pure FeTi	FeTi	Cubic, Pm-3m	98.6 ± 0.4	$a = 2.9788 \pm 0.0004$	Fe: Ti = 1: 1
	$FeTi_2$	Cubic, Fd-3m	1.4 ± 0.1	$a = 11.3067 \pm 0.0035$	Fe: Ti = 1: 2
C45-Gr2 FeTi	FeTi	Cubic, Pm-3m	96.0 ± 0.4	$a = 2.9778 \pm 0.0002$	Fe: Ti = 1: 1
	Fe_2Ti	Hexagonal, P6$_3$/mmc	2.8 ± 0.1	$a = 4.8463 \pm 0.0001$	Fe: Ti = 2: 1
				$c = 7.8710 \pm 0.0005$	
	TiC	Cubic, Fm-3m	1.2 ± 0.1	$a = 4.2847 \pm 0.0003$	Ti: C = 1: 1
316L-Gr2 FeTi	FeTi	Cubic, Pm-3m	49.3 ± 0.3	$a = 3.1057 \pm 0.0004$	Fe: Cr: Ni: Ti = 7: 2: 1: 10
	CrFeTi	Hexagonal, P6$_3$/mmc	31.3 ± 0.4	$a = 5.0476 \pm 0.0001$	Fe: Cr: Ti = 2: 1: 2
				$c = 8.2099 \pm 0.0001$	
	$Fe_{0.2}Ti_{0.8}$	Cubic, Im-3m	19.4 ± 0.8	$a = 3.1013 \pm 0.0001$	Fe: Cr: Ni: Ti = 5: 2: 2: 16
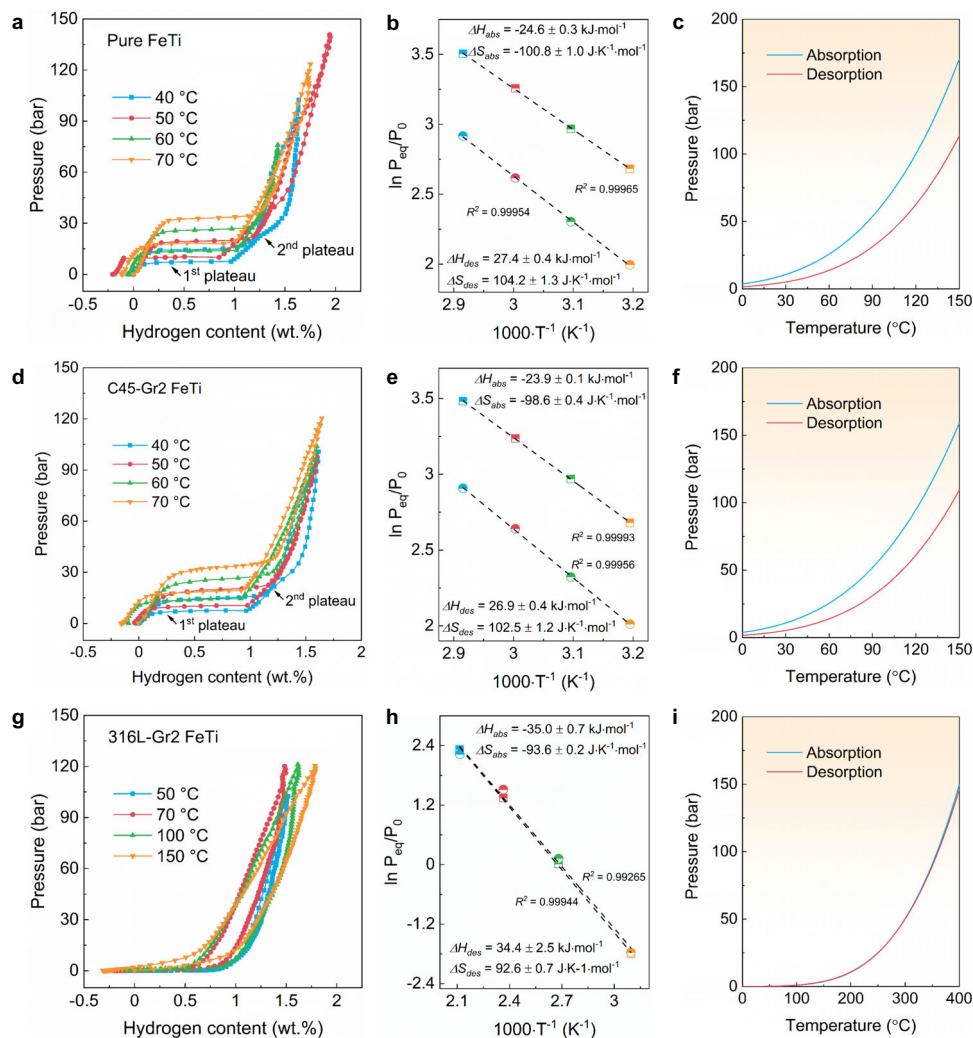
Fig. 3 Reversible hydrogen storage capacities of pure FeTi, C45-Gr2 FeTi, and 316L-Gr2 FeTi alloys. a PCI curves (at 40 °C, 50 C, 60 °C, and 70 °C), **b** van't Hoff plots of hydrogenation/dehydrogenation, and **c** P-T diagram of pure FeTi. **d** PCI curves (at 40 °C, 50 C, 60 °C, and 70 °C), **e** van't Hoff plots of hydrogenation/dehydrogenation, and **f** P-T diagram of C45-Gr2 FeTi. **g** PCI curves (at 50 °C, 70 C, 100 °C, and 150 °C), **h** van't Hoff plots of hydrogenation/dehydrogenation, and **i** P-T diagram of 316L-Gr2 FeTi alloys.

respectively (Fig. 3h). This reveals that the hydrogenated 316L-Gr2 FeTi is thermodynamically more stable than the pure FeTi and the coexistence of β-phase and γ-phase can not be observed. The ΔH and ΔS values for hydrogenation/dehydrogenation of all three alloys are summarized in Table 2. The hysteresis phenomenon referring to the absorption plateau is higher than the desorption plateau, which is normally not desired for practical applications. By replacing pure Fe and Ti with C45 and Gr2 Ti, the hysteresis does not have a significant

change, as shown in the pressure-temperature (P-T) phase diagram (Fig. 3c, f), reflecting the gap between absorption and desorption does not change significantly. Surprisingly, there is no hysteresis for the 316L-Gr2 FeTi, evidenced by the overlapped absorption and desorption curves in Fig. 3i.

In-situ dehydrogenation behaviors. To investigate the influence of the material composition on the hydrogen storage process, in-

Table 2 Thermodynamic properties of pure FeTi, C45-Gr2 FeTi, and 316L-Gr2 FeTi alloys.

Alloy	Absorption ΔH (kJ mol^{-1})	Absorption ΔS (kJ K^{-1} mol^{-1})	Desorption ΔH (kJ mol^{-1})	Desorption ΔS (kJ K^{-1} mol^{-1})
Pure FeTi	−24.6 ± 0.3	−100.8 ± 1.0	27.4 ± 0.4	104.2 ± 1.3
C45-Gr2 FeTi	−23.9 ± 0.1	−98.6 ± 0.4	26.9 ± 0.4	102.5 ± 1.2
316L-Gr2 FeTi	−35.0 ± 0.7	−93.6 ± 0.2	34.4 ± 2.5	92.6 ± 0.7
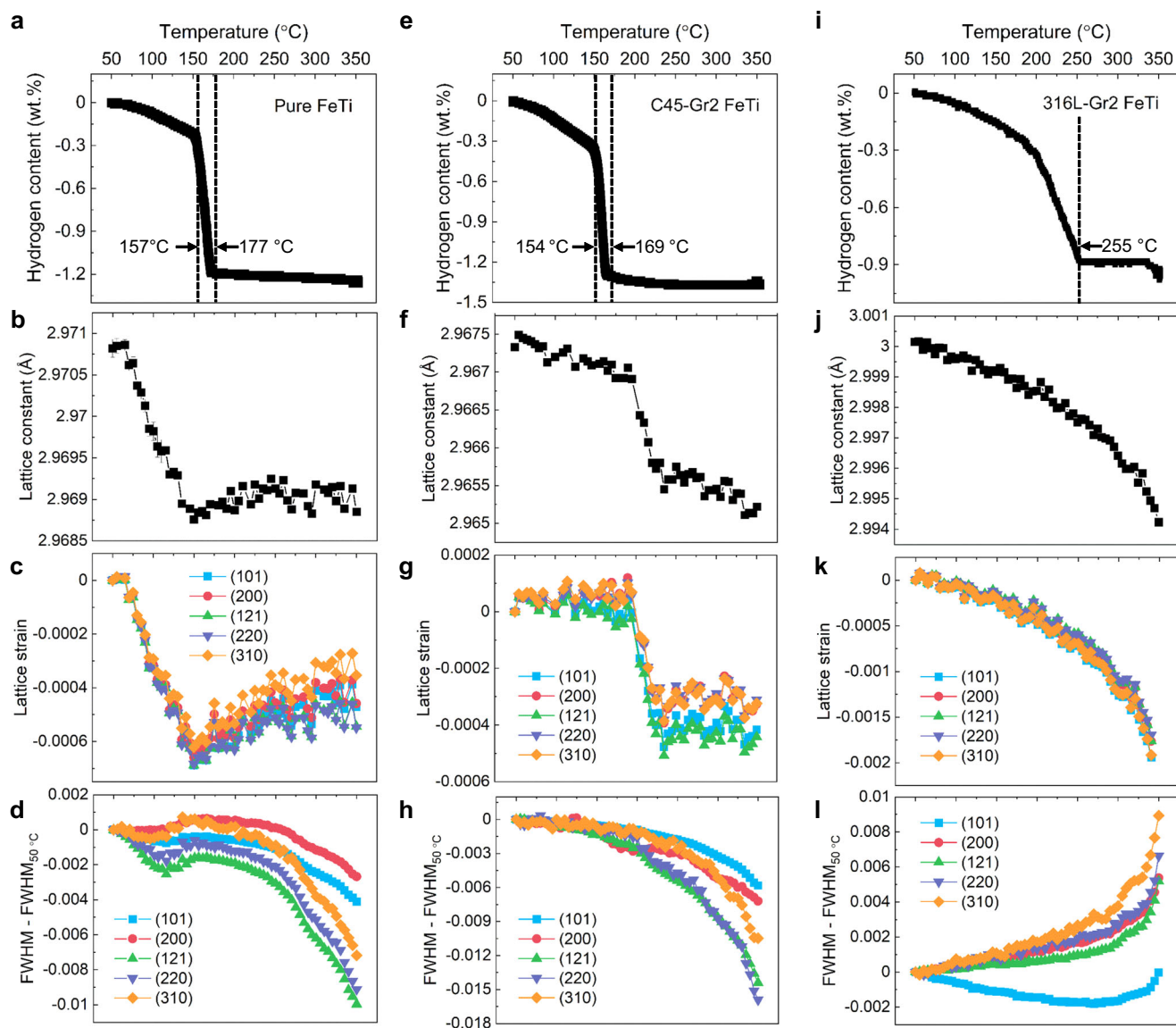
Fig. 4 Dehydrogenation behaviors and corresponding in-situ SR-PXD ($\lambda = 0.20734$ Å) results of pure FeTi, C45-Gr2 FeTi, and 316L-Gr2 FeTi alloys. Backpressure for pure FeTi and C45-Gr2 FeTi is 40 bar, and for 316L-Gr2 FeTi is 10 bar. **a** Volumetric hydrogen capacity, and corresponding, **b** lattice constant, **c** lattice strain, and **d** FWHM changes during in-situ SR-PXD measurements for the pure FeTi powders. **e** volumetric hydrogen capacity, and corresponding **f** lattice constant, **g** lattice strain, and **h** FWHM changes during in situ SR-PXD measurements for the C45-Gr2 FeTi powders. **i** volumetric hydrogen capacity, and corresponding **j** lattice constant, **k** lattice strain, and **l** FWHM changes during in-situ SR-PXD measurements for the 316L-Gr2 powders.

situ synchrotron radiation powder X-ray diffraction (SR-PXD) measurements were carried out on the three alloys. As can be seen in Fig. 4a, 1.25 wt.% of H$_2$ can be desorbed under 40 bar H$_2$ pressure when the pure FeTi is heated from 50 °C to 350 °C. The calculated lattice constant (Fig. 4b) follows the trend of hydrogen content in pure FeTi, indicating that hydrogen slightly induces lattice expansion for the pure FeTi, whereas the effect of hydrogen on the lattice constant is around 1.74×10^{-3} Å wt.%$^{-1}$ of H$_2$.

While by giving a focus on the lattice strain for different planes in Fig. 4c, the conclusion that the lattice strain change is not dependent on the grain orientations can be obtained, since no big differences in lattice strain can be found among different planes. In Fig. 4d, the (121) plane exhibits the largest change of full width at half maximum (FWHM), while the (200) plane has the smallest change, indicating the density of defects or internal stress is changed anisotropically. Similarly, as shown in Fig. 4e, f, for the
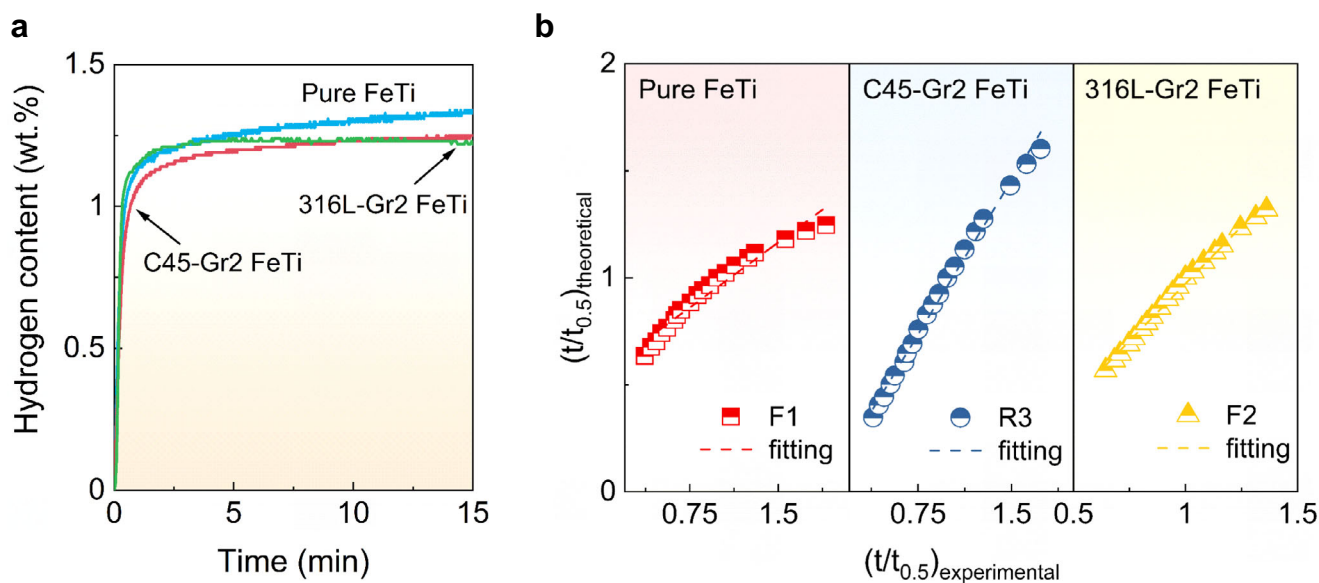
Fig. 5 Hydrogenation kinetic behaviors at 40 °C and under 65 bar of H$_2$ pressure of pure FeTi, C45-Gr2 FeTi, and 316L-Gr2 FeTi alloys. a Volumetric hydrogen capacities for hydrogenation of pure FeTi, C45 FeTi, and 316 L FeTi alloys. **b** corresponding kinetic modeling results of pure FeTi, C45-Gr2 FeTi, and 316L-Gr2 FeTi alloys.

C45-Gr2 FeTi, around 1.36 wt.% of H$_2$ can be released, and the lattice constant decreases during the dehydrogenation process. However, when the temperature reaches 250 °C, the hydrogen content does not change anymore, but the lattice constant still changes. The calculated hydrogen effect on the lattice constant is 1.43×10^{-3} Å wt.%$^{-1}$ of H$_2$. The lattice strain change (Fig. 4g) for different planes also has the same trend as the hydrogen content change, and no significant difference can be found among various planes. For the FWHM shown in Fig. 4h, the (121) and (220) planes show the largest change, and the (101) plane exhibits the smallest change. In Fig. 4i, it is shown that the total dehydrogenation capacity of 316L-Gr2 FeTi alloy is 0.98 wt.% of H$_2$, and upon hydrogenation the lattice constant (Fig. 4j) changes continuously, leading to lattice variation of 2.89×10^{-3} Å wt.%$^{-1}$ of H$_2$. Similar to the pure and C45-Gr2 FeTi alloys, the lattice strain of all planes for 316L-Gr2 FeTi has a similar trend, as exhibited in Fig. 4k. In contrast, the FWHM of 316L-Gr2 FeTi (Fig. 4l) increases with the decrease of hydrogen content, indicating the defects and internal stress in this alloy show the opposite behavior compared to the pure and C45-Gr2 FeTi alloys. The (310) plane has the largest change of FWHM, and the (101) has the smallest change. The results indicate that during the dehydrogenation process, elastic anisotropic behavior is not clearly seen, but the density of defects and internal stress anisotropy is significant.

Kinetic modeling. To understand the effects of phase composition on the hydrogen storage properties, the kinetic performance of the three alloys were measured, as shown in Fig. 5a. The results show that at 40 °C and under 65 bar of H$_2$ pressure, 1.33 wt.% of H$_2$ can be absorbed by the pure FeTi in 10 min, whereas 1.25 wt.% of H$_2$ can be absorbed by C45-Gr2 and 316L-Gr2 FeTi alloys under the same conditions. Note that the measurements of the kinetics data are sample-dependent (particle size, number of cycles) and are strongly influenced by the heat management/temperature control to achieve stabilization of the temperature conditions. Kinetic modeling was used to determine the rate-limiting step during the hydrogenation process of the investigated alloys[36]. As can be seen from Fig. 5b and Supplementary Tables 4–6, the matched kinetic models for pure, C45-Gr2, and

316L-Gr2 FeTi alloys are F1, R3, and F2, respectively. The F1 model indicates that the rate-limiting step for pure FeTi is one-dimensional growth-controlled. This model is called Johnson-Mehl-Avrami (JMA) model and it has a dimensional factor $n = 1$, as can be seen in Eq. (1)[37]:

$$[-\ln(1-\alpha)]^{1/n} = kt \qquad (1)$$

where α is the reaction fraction, t is time, and k is a rate constant. By fitting with the experimental data, the obtained k value is 0.0515 s^{-1}. This means that the rate-limiting step could be grain boundary nucleation of the hydride phase after saturation, the growth of needle and plate-shaped hydride phase, or the thickening of long cylinder/needle-shaped hydride phase. However, further research is still required to determine precisely what is the mechanism of the aforementioned processes[37].

As for the C45-Gr2 FeTi, the R3 model shows that the rate-limiting step is the three-dimensional growth of the hydride phase, in which the phases like FeTi, Fe$_2$Ti, or TiC could act as barriers to the growth of the new phase. The contracting sphere/cube model can be described as following[36]:

$$1 - (1-\alpha)^{\frac{1}{3}} = kt \qquad (2)$$

of which the calculated k for the R3 model is 0.0127 s^{-1}. This means that the nucleation of the new phase occurs rapidly on the surface, and the reaction is controlled by the movement of the interface.

Regarding the 316L-Gr2 FeTi, the fitted kinetic model is F2, which means that the reaction rate is controlled by the two-dimensional growth of the hydride phase. The F2 model corresponds to the JMA model with a dimensional factor of $n = 2$, as can be seen in Eq. (1). The calculated k is 0.0742 s^{-1}. With $n = 2$, the rate-limiting step of the reaction can be attributed to one of the following processes: grain edge nucleation; and all shapes growing from dimensions with a decreasing nucleation rate[37]. Similar to the case of pure FeTi, further investigations such as in-situ TEM measurements are needed to really determine the rate-limiting step. Nevertheless, The FeTi, CrFeTi (elemental composition of Cr$_{0.2}$Fe$_{0.4}$Ti$_{0.8}$), and Fe$_{0.2}$Ti$_{0.8}$ (elemental composition of Fe$_{0.2}$Cr$_{0.08}$Ni$_{0.08}$Ti$_{0.64}$) phases could restrict the grain edge nucleation or growth of the hydride phase.
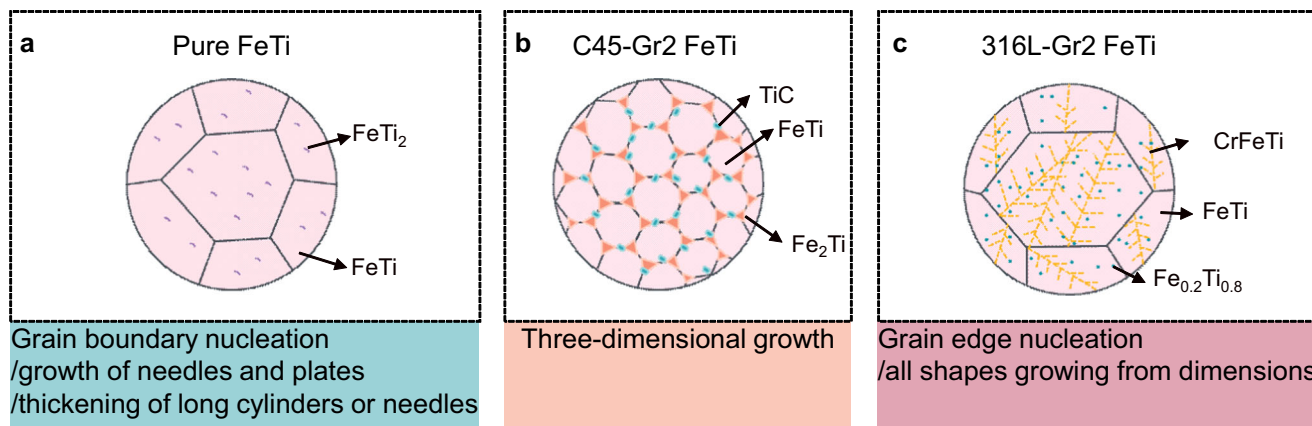
Fig. 6 Schematic sketches illustrating the hydrogenation mechanism of pure FeTi, C45-Gr2 FeTi, and 316L-Gr2 FeTi alloys. a hydrogenation mechanism of pure FeTi. **b** hydrogenation mechanism of C45-Gr2 FeTi. **c** hydrogenation mechanism of 316L-Gr2 FeTi.

Discussion

Here, we reported that by using low-purity recycled alloys, e.g. C45 steel contains around 0.45 wt.% of C, whereas 316 L steel can have a content of Ni between 10 to 14 wt.%, 16 to 18 wt.% of Cr (316 L), and Ti alloy contains around 0.25 wt.% of O (3.7035 Titanium Grade 2), FeTi alloys that absorb hydrogen similarly (in wt.%) to pure FeTi can be obtained, as shown in Fig. 3. However, if we look at the thermodynamic properties (as shown in the plateaus on the PCI curves), the use of different steels leads to considerable changes in stability. The sample prepared from 316 L has a plateau pressure notably lower than that of pure FeTi, indicating that the thermodynamic properties of the alloy have been modified. For practical application, the possibility of modifying the plateau pressure by using different steel sources might be a powerful tool for tuning the thermodynamic properties of FeTi alloy. The SEM and TEM analysis of C45-Gr2 FeTi indicates that besides the matrix of FeTi, phases of Fe_2Ti and TiC are present (Fig. 1d–f), and the hydrogenation reaction is controlled by the three-dimensional growth of the hydride phase (Fig. 6). In literature it is reported that the addition of 0.1 at.% of C to FeTi[33] leads to the formation of Fe_2Ti, and Ti besides FeTi. In addition, a reduction of the hydrogen storage capacity from 1.55 wt.% (pure FeTi) to 1.17 wt.% is expected to occur at 40 °C. These findings indicate that if carbon atoms are located in the interstitial sites of an array of two Fe atoms and four Ti atoms in FeTi, large lattice expansion or strain will be caused since the atomic diameter of carbon is more than two times larger than the width of the octahedral site in FeTi. Then the size of other interstitial sites for hydrogen will be varied and decreased, thus affecting the hydrogen storage capacity[33]. However, in the C45-Gr2 FeTi investigated in the present work, the C present in the system (around 2.1 at.%) appears to interact with Ti forming TiC. The formed Fe_2Ti is distributed at the boundary of FeTi grains with a triangular shape, while the TiC has a smaller particle size and is as well distributed near the grain boundary. These two phases suppress the grain growth of the FeTi phase during the casting process, which helps achieve a fine microstructure and extended grain boundary regions. These grain boundaries, normally are locations with high energy, which are beneficial for hydrogen absorption. Therefore, the hydrogen storage properties do not decrease excessively for the C45-Gr2 FeTi when being compared with pure FeTi. The main phase composition in the 316L-Gr2 FeTi is $(Fe_{0.7}Cr_{0.2}Ni_{0.1})Ti$, indicating that the Ni and Cr substitute Fe partially, and small amounts of CrFeTi (elemental composition of $Cr_{0.2}Fe_{0.4}Ti_{0.8}$) and $Fe_{0.2}Ti_{0.8}$ (elemental composition of $Fe_{0.2}Cr_{0.08}Ni_{0.08}Ti_{0.64}$) can also be found. The presence of Ni and Cr decreases the plateau pressure and reduces the hysteresis of the

PCI curves (Fig. 3g), as compared with pure FeTi (Fig. 3a), which thermodynamically stabilizes the hydride phase. As reported in the literature, by substituting Fe with Cr and Ni, the first plateau pressure will be lowered. Meanwhile, the second plateau will be suppressed by the introduction of Cr, and shifted to higher pressures by the substitution with Ni[38–40]. For example, Mintz et al. showed that by substituting Fe in FeTi with Ni, at 50 °C, the first plateaus of the $Fe_{0.8}TiNi_{0.2}$ alloy for absorption and desorption are at around 0.3 and 0.25 bar, respectively[39]. Li et al. reported that the first plateau pressure decreases with the increasing of Ni content[38]. Furthermore, the presence of Ni and Cr can reduce the hysteresis between absorption and desorption plateaus. For example, at 50 °C, the equilibrium pressures of our 316L-Gr2 FeTi are 0.17 bar for absorption and 0.16 bar for desorption, which are in good agreement with the reported effects of Cr and Ni[41,42]. Our results indicate that under the synergistic effect of Ni and Co, the first plateau pressure can be lowered and the second plateau vanishes, offering a possible strategy for tuning the material thermodynamic properties by selecting steels containing different amounts of Cr and Ni.

The hydrogenation mechanism of these three alloys is summarized in Fig. 6. In the as-synthesized pure FeTi, the present phases are FeTi and $FeTi_2$, and the rate-limiting step for the hydrogenation is one among grain boundary nucleation of the hydride phase after saturation, growth of needle and plate shaped hydride phases, and the thickening of long cylinder/needle shaped hydride phases (Fig. 6a). For the C45-Gr2 FeTi, the existence of the phases Fe_2Ti and TiC might have influenced the hydrogenation process, leading to a change in the rate-limiting step to three-dimensional growth of the hydride phase (Fig. 6b). Elements such as Ni and Cr in 316L-Gr2 FeTi could provide a channel for hydrogen to be absorbed into the phase, affecting the hydrogenation rate and changing the rate-limiting step of the hydrogenation reaction to either grain edge nucleation or all shapes growing from dimensions with a decreasing nucleation rate of the hydride phase, i.e. the monohydride (β-phase), as can be seen in Fig. 6c. This nucleation or growth nature could suppress the phase transition from β-phase to γ-phase, thus affecting the hydrogen storage performance.

For our materials, the larger the lattice constant, the lower the equilibrium pressure[1]. For example, the obtained hydrogenation equilibrium pressures for pure FeTi, C45-Gr2 FeTi, and 316L-Gr2 FeTi at 50 °C are 19.4,19.5, and 0.17 bar, respectively (Fig. 3a, d, g), and the corresponding lattice constants of the alloys are $a = 2.9788 \pm 0.0004$, 2.9778 ± 0.0002, and 3.1057 ± 0.0004 Å, respectively (Table 1). Although the equilibrium pressure may have some correlations with the lattice constant, it is still hard to
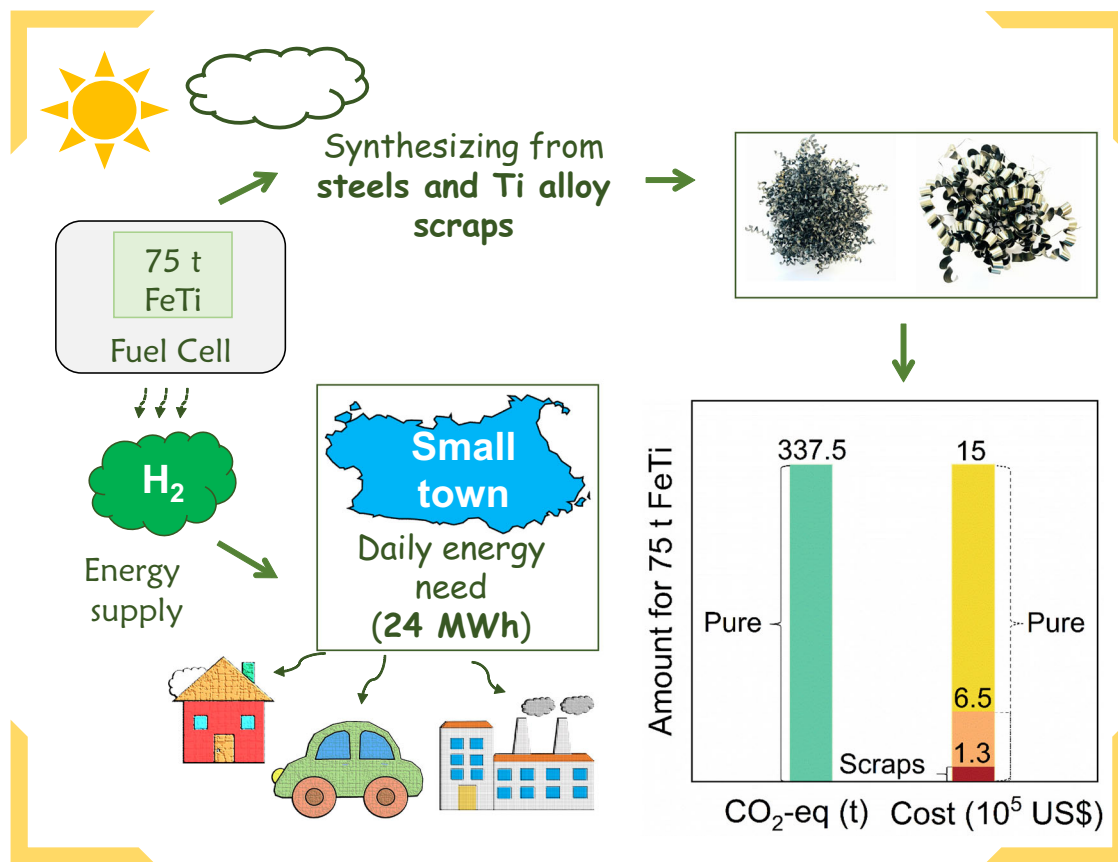
Fig. 7 Schematics for utilizing hydrogen contained in FeTi to store the daily energy needed for a small community. The CO_2-eq and cost reduction achieved by utilizing FeTi obtained from metal scraps instead of high-purity Fe and Ti is provided in the column chart.

define and predict those by knowing the alloy composition for the TiFe phase. Further attempts may be made with the help of computational methods such as high-throughput screening and machine learning.

In addition, by changing the sources of the Fe, the activation process for the FeTi alloys also changes. As an example, the duration of the activation process under 65 bar of H_2 atmosphere and at 50 °C decreases from 38 h for pure FeTi to 18 h for the 316L-Gr2 FeTi, as shown in Supplementary Fig. 7a. On the contrary, the time to fully activate the C45-Gr2 FeTi is 68 h (see Supplementary Fig. 7b). Elements like Ni and Cr (contained in the 316 L) are known to exert a positive effect on the activation of FeTi alloys[11]. Differently from what was previously reported in the literature, the presence of C in C45-Gr2 FeTi, appears to hinder the activation process[11].

The use of metal waste as a raw material source instead of highly pure metals for the FeTi synthesis certainly allows a reduction in the FeTi carbon footprint. Aiming at quantifying such a reduction, we can take as an example a small town where the daily electricity need is about 24 MWh[43]. Given that hydrogen has an energy density of about 120 MJ kg^{-1}, 720 kg of hydrogen could meet this demand. However, when considering the yield of conversion of PEM fuel cells, which is around 40 ~ 80%[44,45], at least 900 kg of hydrogen would be required. Considering that a modern electrolyzer delivers hydrogen at a pressure between 30 and 50 bar, which is the pressure at which the synthesized FeTi system's gravimetric hydrogen capacity is about 1.2 wt.% (Fig. 3d, g), it takes ca. 75 t of C45-Gr2 FeTi or 316L-Gr2 to store 900 kg of hydrogen. We can now calculate how many CO_2-eq would be released if high-purity Fe and Ti sources were replaced with scraps of steel and Ti alloys, ignoring the amount of

CO_2-eq associated with the synthesis of the alloys (which is the same for the FeTi obtained from high-purity sources and from scrap materials), and concentrating our attention on the production of the stating sources, i.e. Fe and Ti. For 1 kg of FeTi, the value is calculated to be $1.5 \times 55.845/(55.845 + 47.867) + 8.1 \times 47.867/(55.845 + 47.867) = 4.5$ kg CO_2-eq kg^{-1}, so for producing 75 t C45-Gr2 FeTi or 316L-Gr2 FeTi, the carbon footprint will be reduced by 337.5 t CO_2-eq, as shown in Fig. 7.

Furthermore, the use of metal scraps as a raw material could considerably lower the cost of the FeTi that is produced. Taking into account that the price of high-purity Fe[24] is 7 US\$ kg^{-1} and that of high-purity Ti[25,26] lies between 10.5 and 35.3 US\$ kg^{-1}, the material cost necessary for producing 75 t FeTi falls in the range between 6.5×10^5 and 1.5×10^6 US\$. The price for steel scrap[46] is ~0.4 US\$ kg^{-1}, whereas the price of Ti alloy scrap[47] is ~3.3 US\$ kg^{-1}. Therefore, the raw material cost to be covered to produce 75 t FeTi from metal scraps, might be as low as 1.3×10^5 US\$ (between 80% and 91.3% lower than using high-purity Fe and Ti) (Fig. 7).

Conclusion

In this study, we demonstrated a strategy for developing sustainable and cost-competitive FeTi alloys for hydrogen storage using recycled C45 and 316 L steels and Ti Grade 2 alloy. Astonishingly, at 50 °C and 100 bar of H_2, the hydrogen storage capacities measured for the FeTi alloys synthesized from recycled scraps are 1.61 wt.% (C45-Gr2 FeTi) and 1.50 wt.% (316L-Gr2 FeTi), which are extremely close to the value measured for the pure FeTi (1.70 wt.%). The close proximity between the measured hydrogen storage capacities of the FeTi alloys obtained from

recycled material and pure elements is maintained for the overall investigated temperature and hydrogen pressure ranges. The microstructural characterization of the alloys shows that except for the FeTi matrix, Fe_2Ti and TiC are present in the C45-Gr2 alloy, whereas CrFeTi (elemental composition of $Cr_{0.2}Fe_{0.4}Ti_{0.8}$) and $Fe_{0.2}Ti_{0.8}$ (elemental composition of $Fe_{0.2}Cr_{0.08}Ni_{0.08}Ti_{0.64}$) were presented in the 316L-Gr2 alloy. The PCI results indicate that the impurities in the starting materials can help to modify the thermodynamic stability of the FeTi alloy without deteriorating the hydrogen storage capacity. Our attempt demonstrates the feasibility of tuning properties by selecting different steels and Ti alloys, which can furtherly be extended to other steels and titanium alloys sources. In addition, by using steels and Ti alloy scraps instead of high-purity Fe and Ti, the FeTi carbon footprint and cost can be tremendously reduced. This work proves that using steel and Ti alloy scraps instead of high-purity Fe and Ti to synthesize high-performance FeTi-based alloys for hydrogen is possible and thus opens a path to the development of environmentally sustainable alloys for hydrogen storage purposes.

Methods

Materials preparation.
Four grams of Fe foil (99.5% purity, Sigma-Aldrich) and Ti foil (99.7% purity, Alfa Aesar) for pure FeTi, C45 steel, and 3.7035 Titanium Grade 2 for C45-Gr2 FeTi, 316 L steel, and 3.7035 Titanium Grade 2 for 316L-Gr2 FeTi, with an atomic ratio of 1:1 were melted together by an Edmund Buhler MAM-1 arc melter, and the ingots were re-melted five times to ensure their homogeneity. The obtained ingots were then suction-cast to rods with a dimension of Φ3 mm × 30 mm. The rods were hand-crushed inside an Ar-filled glovebox (H_2O and O_2 levels < 1 ppm), and a 125 μm sieve was used to sieve the powders. The activation processes were as the followings: first, the sample was put under a dynamic vacuum at 90 °C for 15 h, then the sample temperature was decreased to 50 °C, and 65 bar of H_2 pressure was charged to the sample. If the sample does not absorb hydrogen in 18 h, heat the sample back to 90 °C and evacuate for an extra 3 h. Then decrease the temperature again to 50 °C and load 65 bar of H_2 pressure to the samples and keep it for at least 20 h to activate the samples. To ensure that all the samples are fully activated, 10 additional hydrogenation/dehydrogenation cycles were performed, the conditions for hydrogenation are 50 °C, 60–65 bar of H_2, and for dehydrogenation are 50 °C, 1 bar of H_2.

Microstructure characterization.
HEXRD measurements of the bulk FeTi alloys were performed at beamline HEMS run by Helmholtz-Zentrum hereon GmbH at PETRA III of Deutsches Elektronen-Synchrotron (DESY), Hamburg, Germany. The selected wavelength was $\lambda = 0.124$ Å. The sample-to-detector distance (SDD) was calibrated by using a LaB_6 standard sample from NIST. The obtained 2D images were converted to numerical data via FIT2D[48] software. Afterwards, the MAUD[49] program was used to identify the phase constitution and lattice constant.

SEM characterizations of the bulk FeTi alloys were conducted at a Field Emission Scanning Electron Microscopy (FE-SEM, Zeiss Auriga, and LEO Gemini). The rods were embedded into fast-curing resins along the casting direction, then the sample was ground and mechanically polished.

To investigate the phase constitutions of the alloys, the focused ion beam (FIB) lift-out technique was used to prepare TEM samples. The samples were first thinned by using 30 keV Ga^+ and polished by decreasing ion energy gradually down to 2 keV for mitigating artificial damage. TEM measurements were performed with a JEM-2100F TEM operating at 200 kV. The elemental distribution of the samples was characterized using the EDX capabilities of the TEM.

Hydrogen storage properties.
All the samples used for investigating volumetric properties were prepared and handled inside the glovebox. The PCI measurements at each temperature (40 °C, 50 °C, 60 °C, and 70 °C for pure FeTi and C45-Gr2 FeTi, 50 °C, 100 °C, 150 °C, and 200 °C for 316L-Gr2 FeTi) were performed at a PCT-Pro 2000 Setaram & Hy-Energy manometric Sievert type apparatus. The temperatures chosen for 316L-Gr2 FeTi are higher because the plateaus were shifted to lower pressure for this alloy. The hydrogenation/dehydrogenation ΔH and ΔS were calculated by fitting the experimental data at different temperatures via van't Hoff equation:

$$\ln \frac{P_{eq}}{P_0} = \frac{\Delta H}{RT} - \frac{\Delta S}{R} \qquad (3)$$

where P_{eq} is the equilibrium pressure obtained from PCI curves for hydrogenation/dehydrogenation, P_0 is the standard pressure, T is temperature, and R is the gas constant. Based on the fitting results, the hydrogenation/dehydrogenation ΔH and ΔS can be obtained from the slope and the y-intercept, respectively. The errors on the hydrogenation/dehydrogenation ΔH and ΔS values are obtained from the fitting errors of the slope and the y-intercept.

The hydrogenation kinetic measurements were investigated via a custom-built in-house Sieverts-type apparatus. Around 200 mg of materials were loaded into the sample holder inside the glovebox, and the measurements were performed at 40 °C and under 65 bar of H_2 pressure. The dehydrogenation behaviors were also determined on a custom-built in-house Sieverts-type apparatus. The samples were heated from 50 °C to 350 °C with a heating rate of 5 °C min^{-1}, while the pure FeTi and C45-Gr2 FeTi were dehydrogenated under 40 bar of H_2 pressure, and the 316L-Gr2 FeTi was dehydrogenated under 10 bar of H_2 pressure.

In situ SR-PXD measurements.
The microstructure changes of the powdered alloys after activation during the dehydrogenation process were characterized by utilizing in-situ SR-PXD, which was carried out at beamline P02.1 at PETRA III of DESY, Hamburg, Germany. The utilized wavelength was $\lambda = 0.20734$ Å and the used detector is Varex 4343CT. The powder was loaded into a sapphire capillary and then attached to a home-designed high-pressure sample cell[50] inside an Ar-filled glovebox. To observe the dehydrogenation behaviors of the materials, the materials were heated from 50 °C to 350 °C with a heating rate of 5 °C min^{-1} and kept isothermal at 350 °C for 30 min under hydrogen pressure. The hydrogen backpressure for the pure FeTi and C45-Gr2 FeTi was 40 bar, while for the 316L-Gr2 FeTi was 10 bar. To remove the effect of temperature, the same measurements were done under the same temperature program without hydrogen pressure but under 1 bar of Ar. The SSD was calibrated by using a LaB_6 standard from NIST. The data during dehydrogenation was acquired each 10 s and the recorded 2D images were converted into numerical data via FIT2D software[48].

The lattice constant of the matrix for each alloy was calculated by plotting the lattice constant calculated by each peak versus $\frac{\cos^2\theta}{2}\left(\frac{1}{\sin\theta} + \frac{1}{\theta}\right)$[51], of which θ is the Bragg angle. By extrapolating the graph to $\theta = 90°$, the lattice constant can be obtained. The lattice constant was calibrated by subtracting the effect of temperature on the lattice constant for each sample. The lattice strain (ε_{hkl}) of each (hkl) plane was determined from the shift of peak position of (hkl) reflection by the following equation:

$$\varepsilon_{hkl} = \frac{d_{hkl} - d_{hkl}^0}{d_{hkl}^0} \qquad (4)$$

where d_{hkl} is the d-spacing value at the given temperature, and d_{hkl}^0 is the d-spacing value at 50 °C.

Kinetic modeling.
The Sharp and Jones method was used for kinetic modeling[52,53]. In this method, the experimental data can be expressed as follows:

$$F(\alpha) = A\left(\frac{t}{t_{0.5}}\right) \qquad (5)$$

where α is the reacted fraction, t is the reaction time, $t_{0.5}$ is the time at $\alpha = 0.5$, and A is the rate constant. $F(\alpha)$ is the measured hydrogen storage capacity over the overall capacity of the second dehydrogenation step. The portion of the dehydrogenation curve used for this investigation is the one that included between 0.20 and 0.70 of the overall hydrogen storage capacity. Firstly, for the investigated samples, the kinetic curves were normalized. Subsequently, different fitting models[36,54] were used to fit the obtained curves (Supplementary Table 7). The criterion for deciding whether a model successfully describes the desorption reaction is the following: the slope of the fitted curve should be close to 1, the intercept should be close to 0, and the fitting coefficient of determination R^2 should be close to 1.

Data availability
Data supporting the findings of this study are available from the corresponding author upon reasonable request.

References
1. Reilly, J. J. & Wiswall, R. H. Formation and properties of iron titanium hydride. *Inorg. Chem.* **13**, 218–222 (1974).
2. Burzo, E. *Hydrogen storage materials*. Springer (2018).
3. Zhang, Y. H. et al. Research progress of TiFe-based hydrogen storage alloys. *J. Iron Steel Res. Int.* **29**, 537–551 (2022).
4. Pistidda, C. Solid-state hydrogen storage for a decarbonized society. *Hydrogen* **2**, 428–443 (2021).
5. Pasquini, L. et al. Magnesium-and intermetallic alloys-based hydrides for energy storage: modelling, synthesis and properties. *Prog. Energy* **4**, 032007 (2022).
6. Alvares, E. et al. Modeling the thermodynamics of the FeTi hydrogenation under para-equilibrium: an ab-initio and experimental study. *Calphad* **77**, 102426 (2022).

7. Schlapbach, L. & Riesterer, T. The activation of Feti for hydrogen absorption. *Appl. Phys. A* **32**, 169–182 (1983).

8. Lee, J. Y., Park, C. N. & Pyun, S. M. The activation processes and hydriding kinetics of FeTi. *J. Less Common Met.* **89**, 163–168 (1983).

9. Schober, T. On the activation of FeTi for hydrogen storage. *J. Less Common Met.* **89**, 63–70 (1983).

10. Schober, T. & Westlake, D. G. The activation of FeTi for hydrogen storage - a different view. *Scripta Metall. Mater.* **15**, 913–918 (1981).

11. Dematteis, E. M., Berti, N., Cuevas, F., Latroche, M. & Baricco, M. Substitutional effects in TiFe for hydrogen storage: a comprehensive review. *Mater. Adv.* **2**, 2524–2560 (2021).

12. Dreistadt, D. M. et al. An effective activation method for industrially produced TiFeMn powder for hydrogen storage. *J. Alloy Compd.* **919**, 165847 (2022).

13. Dematteis, E. M. et al. Fundamental hydrogen storage properties of TiFe-alloy with partial substitution of Fe by Ti and Mn. *J. Alloy Compd.* **874**, 159925 (2021).

14. Jung, J. Y., Lee, Y. S., Suh, J. Y., Huh, J. Y. & Cho, Y. W. Tailoring the equilibrium hydrogen pressure of TiFe via vanadium substitution. *J. Alloy Compd.* **854**, 157263 (2021).

15. Sandrock, G. D. The metallurgy and production of rechargeable hydrides. In: *Hydrides for energy storage.* Elsevier (1978).

16. Sujan, G. K., Pan, Z. X., Li, H. J., Liang, D. & Alam, N. An overview on TiFe intermetallic for solid-state hydrogen storage: microstructure, hydrogenation and fabrication processes. *Crit. Rev. Solid State* **45**, 410–427 (2020).

17. GKN Hydrogen. <https://www.gknhydrogen.com/#app> (2022).

18. Kuziora, P., Kunce, I., McCain, S., Adkins, N. J. E. & Polanski, M. The influence of refractory metals on the hydrogen storage characteristics of FeTi-based alloys prepared by suspended droplet alloying. *Int. J. Hydrog. Energy* **45**, 21635–21645 (2020).

19. Zaluski, L., Zaluska, A., Tessier, P., Stromolsen, J. O. & Schulz, R. Effects of relaxation on hydrogen absorption in Fe-Ti produced by ball-milling. *J. Alloy Compd.* **227**, 53–57 (1995).

20. Kumar, S., Tiwari, G. P., Sonak, S., Jain, U. & Krishnamurthy, N. High performance FeTi-3.1 mass % V alloy for on board hydrogen storage solution. *Energy* **75**, 520–524 (2014).

21. Sandrock, G. D., Reilly, J. J. & Johnson, J. R. Metallurgical considerations in the production and use of FeTi alloys for hydrogen storage. Brookhaven National Lab., Upton, NY (USA) (1976).

22. Lv, P. & Huot, J. Hydrogen storage properties of Ti0.95FeZr0.05, TiFe0.95Zr0.05 and TiFeZr0.05 alloys. *Int. J. Hydrog. Energy* **41**, 22128–22133 (2016).

23. Haraki, T. et al. Properties of hydrogen absorption by nano-structured FeTi alloys. *Int. J. Mater. Res* **99**, 507–512 (2008).

24. Li, B., Sun, G. Y., Li, S. Y., Guo, H. J. & Guo, J. The preparation of high-purity iron (99.987%) employing a process of direct reduction-melting separation-slag refining. *Materials* **13**, 1839 (2020).

25. Institut Seltene Erden. <https://en.institut-seltene-erden.de/prices-for-high-purity-metals-in-may-2020/> (2022).

26. Asian Metal. <https://www.asianmetal.com/Titanium-Price/> (2022).

27. Nuss, P. & Eckelman, M. J. Life cycle assessment of metals: a scientific synthesis. *Plos One* **9**, 101298 (2014).

28. Yokoi, R., Watari, T. & Motoshita, M. Future greenhouse gas emissions from metal production: gaps and opportunities towards climate goals. *Energy Environ. Sci.* **15**, 146–157 (2022).

29. Raabe, D., Tasan, C. C. & Olivetti, E. A. Strategies for improving the sustainability of structural metals. *Nature* **575**, 64–74 (2019).

30. Souza, I. R. et al. Sustainable steel through hydrogen plasma reduction of iron ore: process, kinetics, microstructure, chemistry. *Acta Mater* **213**, 116971 (2021).

31. Ashby, M. F. *Materials and the environment: eco-informed material choice.* Elsevier (2012).

32. Takeda, O. & Okabe, T. H. Current status of titanium recycling and related technologies. *JOM* **71**, 1981–1990 (2019).

33. Lee, S. M. & Perng, T. P. Effects of boron and carbon on the hydrogenation properties of TiFe and Ti1.1Fe. *Int. Int. J. Hydrog. Energy* **25**, 831–836 (2000).

34. Patel, A. K. et al. Microstructure and first hydrogenation properties of TiFe alloy with Zr and Mn as additives. *Int. Int. J. Hydrog. Energy* **45**, 787–797 (2020).

35. Park, K. B. et al. Characterization of microstructure and surface oxide of Ti1.2Fe hydrogen storage alloy. *Int. Int. J. Hydrog. Energy* **46**, 13082–13087 (2021).

36. Khawam, A. & Flanagan, D. R. Solid-state kinetic models: basics and mathematical fundamentals. *J Phys Chem B* **110**, 17315–17328 (2006).

37. Christian, J. W. *The theory of transformations in metals and alloys.* Newnes (2002).

38. Li, Y. Q. et al. Investigations on gaseous hydrogen storage performances and reactivation ability of as-cast TiFe1-xNix (x=0, 0.1, 0.2 and 0.4) alloys. *Int. J. Hydrog. Energy* **44**, 4240–4252 (2019).

39. Mintz, M., Vaknin, S., Biderman, S. & Hadari, Z. Hydrides of ternary TiFe x M 1− x (M= Cr, Mn, Co, Ni) intermetallics. *J. Appl. Phys.* **52**, 463–467 (1981).

40. Yang, T. et al. Effect of chromium, manganese and yttrium on microstructure and hydrogen storage properties of TiFe-based alloy. *Int. Int. J. Hydrog. Energy* **45**, 12071–12081 (2020).

41. Zadorozhnyy, V. Y., Klyamkin, S. N., Zadorozhnyy, M. Y., Bermesheva, O. V. & Kaloshkin, S. D. Mechanical alloying of nanocrystalline intermetallic compound TiFe doped by aluminum and chromium. *J. Alloy Compd.* **586**, S56–S60 (2014).

42. Shang, H. W. et al. Investigation on gaseous and electrochemical hydrogen storage performances of as-cast and milled Ti1.1Fe0.9Ni0.1 and Ti1.09Mg0.01Fe0.9Ni0.1 alloys. *Int. J. Hydrogen Ener.g* **43**, 1691–1701 (2018).

43. Gates, B. *How to avoid a climate disaster: the solutions we have and the breakthroughs we need.* Knopf (2021).

44. Alaswad, A. et al. Technical and commercial challenges of proton-exchange membrane (PEM) fuel cells. *Energies* **14**, 144 (2021).

45. Appleby, A. J. Fuel cell technology: status and future prospects. *Energy* **21**, 521–653 (1996).

46. London Metal Exchange. <https://www.lme.com/Metals/Ferrous/LME-Steel-Scrap-CFR-Turkey-Platts#Trading+day+summary> (2022).

47. Titanium Exposed. <https://www.titaniumexposed.com/titanium-scrap-price.html> (2022).

48. Hammersley, A. P. FIT2D: an introduction and overview. *European synchrotron radiation facility internal report ESRF97HA02T* **68**, 58 (1997).

49. Lutterotti, L., Matthies, S., Wenk, H. R., Schultz, A. S. & Richardson, J. W. Combined texture and structure analysis of deformed limestone from time-of-flight neutron diffraction spectra. *J. Appl. Phys.* **81**, 594–600 (1997).

50. Bosenberg, U. et al. Characterization of metal hydrides by in-situ XRD. *Int. J. Hydrog. Energ.* **39**, 9899–9903 (2014).

51. Nelson, J. B. & Riley, D. P. An experimental investigation of extrapolation methods in the derivation of accurate unit-cell dimensions of crystals. *Proc. Phys. Soc. Lond.* **57**, 160–177 (1945).

52. Sharp, J. H., Brindley, G. W. & Achar, B. N. N. Numerical data for some commonly used solid state reaction equations. *J. Am. Ceramic Soc.* **49**, 379–382 (1966).

53. Jones, L. F., Dollimore, D. & Nicklin, T. Comparison of experimental kinetic decomposition data with master data using a linear plot method. *Thermochim. Acta* **13**, 240–245 (1975).

54. Gizer, G. Role of additives on the kinetic and thermodynamic properties of Mg (NH2) 2+ LiH reactive hydride composite. Thesis (2020).

Acknowledgements

Author contributions
Y.S. and C.P. conceived the idea, developed the outline, designed the experiment, and compiled the manuscript. Y.S. conducted the experiments and tests with the assistance of S.L., Z.L., F.P., Z.L., T.H., A.S., J.K., and G.G. M.D., T.K., and C.P. supervised the project.

Funding

Competing interests
The authors declare no competing interests.

Additional information
Supplementary information The online version contains supplementary material available at https://doi.org/10.1038/s43246-022-00324-5.

Correspondence and requests for materials should be addressed to Claudio Pistidda.

Peer review information *Communications Materials* thanks Volodymyr Yartys, Xin Fu Tan, Erika Michela Dematteis, and the other, anonymous, reviewer(s) for their contribution to the peer review of this work. Primary Handling Editors: Jet-Sing Lee and John Plummer. Peer reviewer reports are available.

Reprints and permission information is available at http://www.nature.com/reprints

Publisher's note Springer Nature remains neutral with regard to jurisdictional claims in published maps and institutional affiliations.